

## COMPARISON OF RADAR AND THERMOACOUSTIC TECHNIQUES IN MICROWAVE BREAST IMAGING

G. K. Zhu<sup>1,\*</sup> and M. Popović<sup>2</sup>

<sup>1</sup>Department of Electrical and Computer Engineering, University of Toronto, 10 King's College Road, Toronto, ON M5S 3G4, Canada

<sup>2</sup>Department of Electrical and Computer Engineering, McGill University, 3480 rue Université, Montréal, QC H3A 2A7, Canada

**Abstract**—Microwave radar and microwave-induced thermoacoustic technique exploit the contrast in the permittivity and conductivity between malignant and healthy tissue. They have emerged as promising techniques for detecting breast cancers. This paper compares the imaging capability of these techniques in the presence of homogeneous and heterogeneous breast tissue. Relying on the data from the finite-difference time-domain simulations, the study shows that both techniques are capable of imaging homogeneous objects. In the presence of electromagnetic dispersion and heterogeneity, radar signals suffer from strong dispersion and multiple scattering, which decorrelate the signals with the scatterers. The microwave-induced thermoacoustic technique takes the advantage of breast being acoustically homogeneous and is capable of generating high-quality images.

### 1. INTRODUCTION

Research has shown that the breast malignancy is uniquely correlated with the changes in water content and ionic molecules. This leads to localized changes in permittivity and conductivity at microwave frequencies, which signify higher reflection and absorption of microwave energy [1]. Microwave radar (MR) and microwave-induced thermoacoustics (MITA) have emerged as promising techniques for detecting the breast malignancy. The MR technique exploits the scattered energy due to the change in permittivity and produces images

---

*Received 2 August 2011, Accepted 30 September 2011, Scheduled 4 October 2011*

\* Corresponding author: Guangran Kevin Zhu (kzhu@waves.utoronto.ca).

of the scattered energy as a function of two-dimensional space. The MITA technique exploits the absorbed energy primarily due to the change in conductivity, and produces images of heat absorption as a function of two-dimensional space.

Breast tissue is generally considered electromagnetically dispersive and spatially heterogeneous, and acoustically dispersive and spatially homogeneous. Previous studies of the MR and MITA techniques have focused on cases with significant contrast in the permittivity and conductivity between malignant and healthy tissue and mild tissue heterogeneity. Although the exactly dielectric characteristics of breast tissue in the microwave range have been a subject of debate [2–4], the performance of the MR and MITA technique in the presence of possible tissue heterogeneity deserves more careful analysis.

We used the finite-difference time-domain (FDTD) method to solve Maxwell’s equations and the acoustic wave equations, which gives the radar and thermoacoustic signals in the presence of homogeneous and heterogeneous breast models. We used the delay-and-sum (DAS) algorithm to process both signals and generate breast images.

We found that both the MR and MITA techniques are capable of imaging dielectric inclusions in a homogeneous medium. In particular, the study of including a single inclusion revealed that both techniques are affected by the inclusion size and dielectric contrast. Images from the MR technique have a higher cross-image signal-to-clutter ratio (SCR) than the MITA technique, which suggests that the MR technique is more sensitive to the abrupt change in the dielectric properties. The study involving two inclusions revealed that a reduced dielectric contrast between malignant and healthy tissue can increase the electrical length of the malignant tissue, potentially increasing the spatial resolution achievable by the MR technique. The resolution of MITA images is primarily dependent on the acoustic wavelength and is not related to the variation in the dielectric properties. When we used a heterogeneous breast model built from a magnetic resonance image, the MITA technique was able to reveal the spatial details correlated with the heterogeneity of tissue. Due to the electromagnetic dispersion and tissue heterogeneity, the MR technique could not provide an energy image that correlates with the structure of the tissue.

This paper is structured as follows. Section 2 describes the physics associated with the microwave and thermoacoustic phenomenon. Section 3 summarizes the dielectric, thermal, and acoustic properties of malignant and healthy tissue pertinent to this study. Section 4 describes the DAS algorithm applicable to both imaging techniques. Section 5 discusses the imaging results. Section 6 concludes this work.

## 2. MICROWAVE RADAR AND MICROWAVE-INDUCED THERMOACOUSTICS

The theory associated with the MR technique applied in breast imaging has been summarized in the review paper [5]. Briefly speaking, a pulse with a temporal width on the order of 0.1 ns is generated to probe the breast. The wideband nature of this pulse permits it to resolve small scatterers in space, such as millimeter breast tumors embedded in healthy tissue. The propagation of this pulsed field is governed by Maxwell's equations, which are

$$\frac{\partial \vec{H}}{\partial t} = -\frac{1}{\mu} \nabla \times \vec{E}, \quad (1a)$$

$$\frac{\partial \vec{E}}{\partial t} = \frac{1}{\epsilon} \left( \nabla \times \vec{H} - \vec{J} \right), \quad (1b)$$

where  $\vec{E}$  [V/m] and  $\vec{H}$  [A/m] denote the electric and magnetic field vectors.  $\epsilon$  [F/m] and  $\mu$  [H/m] denote the electric permittivity and magnetic permeability  $\vec{J}$  [A/m<sup>2</sup>] denotes the current density, and  $t$  [s] denotes time. Equation (1) can be collapsed into the wave equation in a homogeneous medium, which is

$$\nabla^2 \vec{E} - \mu \epsilon \frac{\partial^2 \vec{E}}{\partial t^2} = \mu \frac{\partial \vec{J}}{\partial t}. \quad (2)$$

The theory associated with the MITA technique has also been summarized in a number of places (see, for example, [6, 7] and [8]). In brief, to excite the thermoacoustic process in the breast, a pulse-modulated continuous microwave is radiated towards the chest wall. The envelope of the modulating signal is about 1- $\mu$ s wide. The carrier microwave is responsible for depositing energy deep into the tissue. The modulating envelope determines the bandwidth of the thermoacoustic signal.

The amount of the microwave energy deposited in the tissue is quantified by the specific absorption rate (SAR)  $S$  [W/m<sup>3</sup>], which is defined as

$$S = \frac{\sigma_e}{2\rho} |\vec{E}|^2, \quad (3)$$

where  $\rho$  [kg/m<sup>3</sup>] is the mass density and  $\sigma_e$  [S/m] is the effective conductivity. Under the condition of thermal confinement, the SAR can be expressed as the product of a space-dependent term  $\tilde{S}(\vec{r})$  and a unit-less time-dependent term  $I(t)$ , which represents the envelope of the modulated continuous wave, i.e.,  $S = \tilde{S}(\vec{r})I(t)$ . When  $I(t)$  is positive, energy is transferred from the environment to the system.

When  $I(t)$  is negative, energy is transferred from the system to the environment. In the thermoacoustic process,  $I(t)$  stays as a positive quantity, corresponding to the tissue absorption of microwave energy from the environment.

Substituting the time varying SAR to the linear acoustic wave equation [9, pp. 119] leads to

$$\nabla^2 p - \frac{\rho}{K} \frac{\partial^2 p}{\partial t^2} = -\frac{\rho\alpha}{c_p} \frac{\partial}{\partial t} \tilde{S}I, \quad (4)$$

where  $p$  [Pa] denotes the pressure,  $K$  [Pa] denotes the bulk modulus.  $\alpha$  [1/K] is the volume expansion coefficient, and  $c_p$  [J/(kg·K)] is the heat capacity.

Comparing (2) and (4) reveals that the radiated and scattered radar signals are solutions to the inhomogeneous electromagnetic wave equation and the excitation is the current density. The thermoacoustic signals are solutions to the inhomogeneous wave equation. The temperature variation due to the SAR converts every point in space to a pulsating sphere, which becomes the excitation.

The duality of (2) and (4) leads to an almost identical formulation of the FDTD method to model the electromagnetic and acoustic wave propagation and the absorption at the boundaries. The key difference is that the electromagnetic wave is transversal, while the acoustic wave is longitudinal. This fact is reflected in the need of inserting a permutation matrix in the FDTD update equations for the acoustic wave.

### 3. ENDOGENOUS PROPERTIES OF THE HUMAN BREAST

The human breast is an intricate composition of gland, adipose tissue, blood vessels, and skin. The electromagnetic dispersiveness of tissue is commonly described by the Cole-Cole model, which is

$$\epsilon_\infty + \frac{\Delta\epsilon}{1 + (j\omega\tau)^{1-\alpha}} + \frac{\sigma_s}{j\omega\epsilon_o},$$

where  $\epsilon_\infty$  is the relative permittivity for infinite value of frequency, and  $\Delta\epsilon$  is the difference between the infinite and static relative permittivity.  $\tau$  [s] is the relaxation time constant and  $\sigma_s$  [S/m] is the static conductivity. The value of the parameter  $\alpha$  is empirically determined as a correction factor. The Cole-Cole parameters of six typical breast tissue are extracted from [10] for this study, which is based on the data in [2, 3]. They are listed in Table 1 in the order of decreasing adipose content.

**Table 1.** Cole-Cole parameters of the six types of tissue in the order of decreasing adipose content valid from 0.5 GHz to 20 GHz.

Tissue Type	$\epsilon_\infty$	$\frac{\sigma_s}{\text{S/m}}$	$\Delta\epsilon$	$\frac{\tau}{\text{ps}}$	$\alpha$
I	2.908	0.020	1.200	16.88	0.069
II	3.140	0.036	1.708	14.65	0.061
III	4.031	0.083	3.654	14.12	0.055
IV	9.941	0.462	26.60	10.90	0.003
V	7.821	0.713	41.48	10.66	0.047
VI	6.151	0.809	48.26	10.26	0.049
Tumor	9.058	0.899	51.31	10.84	0.022
skin	4.0	0.0002	32	7.23	0
	-	-	1100	32480	0.2

**Table 2.** Acoustic and thermal properties of the breast tissue, tumor, and skin ( $f$  is in MHz.).

	Speed	Density	Atten.	Heat Capacity	Expansion Coeff.
	$c_a$	$\rho$	$\beta$	$c_p$	$\alpha$
	m/s	kg/m <sup>3</sup>	dB/cm	J/(kg·K)	K <sup>-1</sup>
Tissue	1478–1613	990–1060	$0.75f^{1.5}$	2220–3500	$3 \times 10^{-4}$
tumor	1550	1182	$0.57f$	3500	$3 \times 10^{-4}$
skin	1615	1093–1190	0.35	3680	$3 \times 10^{-4}$

The absorption of the microwave energy and conversion to heat in breast tissue are characterized by the volume expansion coefficient  $\alpha$  and the heat capacity  $c_p$ . The tissue density  $\rho$ , acoustic speed  $c_a$ , and acoustic attenuation  $\beta$ , also affect the thermoacoustic signals as they propagate through the tissue. The acoustic and thermal properties of the breast tissue and skin are compiled from [11–17] and listed in Table 2.

The acoustic wave experiences dispersion in the frequency range above 20 kHz, which has been empirically characterized as a function of frequency in several discrete frequency ranges [11]. The linear acoustic attenuation is applicable to the thermoacoustic signals [18]. To capture the dispersion, the quantity “acoustic conductivity”  $\sigma_a$  is introduced to form a dual with the electric conductivity and is related to the acoustic

attenuation through

$$\beta = 20 \log_{10} \left| e^{j\omega \sqrt{\rho/K} \sqrt{1 + \sigma_a K / j\omega}} \right|. \quad (5)$$

To determine the frequency at which we evaluate (5) for the acoustic conductivity, we assume a point source with the envelope  $I$  is excited at some location  $\vec{r}_0$ . The Green's function to (4) in the infinite space is

$$\int_0^t \int_{\Omega} \frac{\rho\alpha}{4\pi c_p} \tilde{S}(\vec{r}') \frac{d}{dt'} I(t') g(\vec{r}, t | \vec{r}', t') d\vec{r}' dt', \quad (6)$$

where  $g(\vec{r}, t | \vec{r}', t')$  denotes the Green's function, and  $\Omega$  denotes the spatial domain of integration. The pressure due to a point source at  $\vec{r}_o$  is

$$\int_0^t \int_{\Omega} \frac{\rho\alpha}{4\pi c_p} \delta(\vec{r}' - \vec{r}_0) \frac{d}{dt'} I(t') g(\vec{r}, t | \vec{r}', t') d\vec{r}' dt', \quad (7)$$

where  $\delta$  denotes the Dirac delta function. Given the Green's function of the two-dimensional wave equation

$$g(\vec{r}, t | \vec{r}', t') = \frac{2c_a}{\sqrt{c_a^2(t-t')^2 - |\vec{r} - \vec{r}'|^2}}, \quad (8)$$

Equation (7) becomes

$$\frac{\rho\alpha}{4\pi c_p} \frac{d}{dt} I \otimes \frac{2}{t}, \quad (9)$$

where  $\otimes$  denotes the temporal convolution. The Fourier transform of (9) gives the spectral content of the signal generated by the point source. We take its peak frequency and use Table 2 to calculate the attenuation, which is then substituted to (5) for the acoustic conductivity via the secant method.

#### 4. DELAY-AND-SUM ALGORITHM

The wave equation remains invariant under the transform  $t \rightarrow -t$  in a lossless medium. This is due to the second-order derivative with respect to time in the equation, which contrasts to the first-order derivative in the diffusion equation. The propagating field at one time instance can be translated to an earlier time to identify its source. This is the basic idea of the DAS algorithm [19, pp. 112]. When the DAS algorithm is applied to the radar signals [20], the pixel intensity of the image is the total energy of the sum of the time-shifted, compensated signals received at the antennas.

The DAS algorithm is equally applicable to thermoacoustic signals with two modifications in contrast to as being applied to the radar

signals. First, only one-way time shift and compensation are needed as the scan point is considered an isotropic acoustic excitation. Second, MITA images represent the heat absorption. As the absorption is linearly related to the amplitude of the thermoacoustic signals, the pixel intensity in a MITA image is the maximum amplitude of the summed signal. MITA images are amplitude images, which contrast to the MR energy images.

## 5. IMAGING RESULTS

In this section, we discuss the quality of images generated with the DAS algorithm from the simulated radar and thermoacoustic signals.

A circular object mimicking a two-dimensional cross-section of a human breast with a radius of 45 mm and a skin thickness of 1.6 mm is placed in oil-like lossless matching medium characterized by the relative permittivity of 4.5. The scenario is shown in Figure 1(a). In the electromagnetic simulation, there are 36 equally-spaced current sources placed around the object 20 mm away from the surface. Each emits a microwave pulse sequentially. This gives 36 mono-static measurements of the scattered field. The minimum wavelength, determined by the largest permittivity in the configuration at 6.85 GHz, is 5.64 mm. We set the spatial increment to 0.4 mm, less than one tenth of the wavelength. The maximum wavelength, determined by the lowest

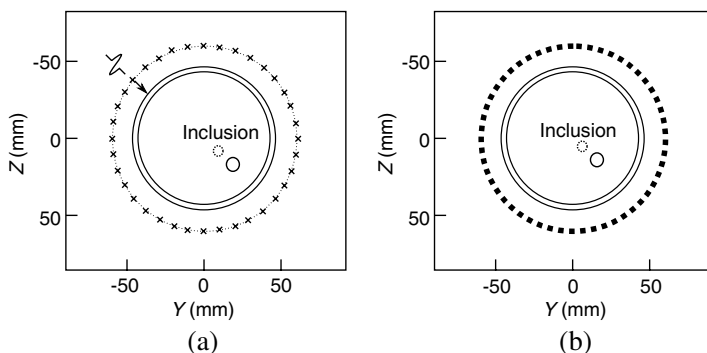


**Figure 1.** (a) A mono-static microwave radar system. There are 36 current sources (marked as “x”) placed 20 mm away from the circular object radiating sequentially. (b) A microwave-induced thermoacoustic system. The object is uniformly excited. There are 80 transducers (marked as “■”) placed 20 mm away from the object simultaneously recording the thermoacoustic signals. The first include is marked in the solid line, while the second inclusion is marked in the dashed line.

permittivity at 3.1 GHz, is 50.3 mm. The simulation domain is truncated by 12 uniaxial perfectly-matched layers placed at half of this wavelength away from the source [21]. The parameters of the perfectly-matched layers are selected by sweeping the possible values of the parameters and monitoring the error of reflection. The computation domain contains  $475 \times 455$  FDTD cells. In the thermoacoustic simulation, we assume the breast is uniformly excited at 550 MHz. There are 80 acoustic transducers placed around the breast as shown in Figure 1(b). At 0.714 MHz, the acoustic wavelength is 2.1 mm. We set the spatial increment to 0.1 mm. The computation domain for the acoustic simulations has  $1500 \times 1420$  FDTD cells.

### 5.1. Homogeneous Medium with One Inclusion

We place one inclusion at (10 mm, 16 mm), and vary its radius and the dielectric properties of the tissue as listed in Table 1. The Debye model that approximates the Cole-Cole model of the tissue in the frequency range from 3.1 GHz to 10.6 GHz is implemented in the numerical simulation. We assume to have the knowledge of the average propagation speed of the electromagnetic wave and acoustic wave inside the tissue. For the electromagnetic wave, it is the speed evaluated at the central frequency and for the acoustic wave, it is 1510 m/s.

The cross-image SCR is defined as the mean energy within the area of 3 dB below the main lobe in the images containing the inclusion and the mean energy within the same area in the images free of the inclusion. Figures 2(a) and 2(b) show the cross-image SCR as

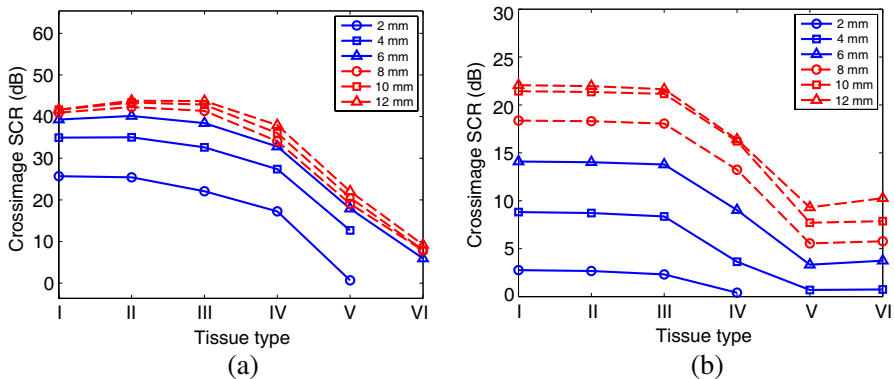


**Figure 2.** Cross-image SCR of (a) radar images and (b) thermoacoustic images. In the extreme cases, the peak of the image deviates from the location of the inclusion. They are subsequently omitted in the plot.

a function of the tissue types and the inclusion diameter. Both the MR and MITA images demonstrate a diminishing SCR as the adipose content decreases or the inclusion size decreases. The decrease of the SCR is not monotonic in the MR images. For instance, when the inclusion is 12 mm in diameter, its electrical size varies from 0.5 to 1.8 with respect to the wavelength at evaluated 6.85 GHz. In this range of the electrical size, the Mie scattering occurs, i.e., scattering occurs strongly or weakly depending on the electrical size. When the inclusion is 2 mm in diameter, its electrical size varies from 0.09 to 0.3 with respect to the wavelength at evaluated 6.85 GHz. The Rayleigh scattering occurs, i.e., the amount of scattered energy is monotonically related to the size of the inclusion. The decrease of the SCR in MITA images is monotonic. This can be explained by the fact that the pixel intensity is linearly related to the contrast in conductivity as evidenced in (6). The slight deviation at the tissue of Type VI is due to the unideal removal of the artifact produced by the background. The MR images have give a higher SCR than the MITA images. This suggests that the MR technique is more sensitive to the abrupt change in the dielectric properties.

## 5.2. Homogeneous Medium with Two Inclusions

Two inclusions are placed at (5 mm, 8 mm) and (10 mm, 16 mm) with diameters of 6 mm and 8 mm respectively. We vary the dielectric properties of the tissue similarly as in the previous analysis. Figure 3(a) shows the MR image when the tissue is of Type III. The two inclusions cannot be resolved. This is because, even though there is a dielectric

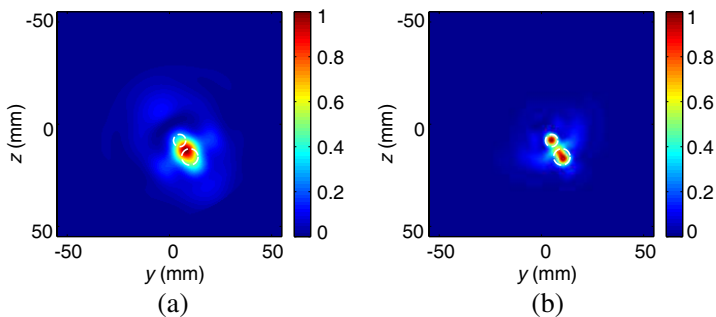


**Figure 3.** MR images generated with the DAS algorithm attempting to resolve two closely spaced inclusions in a homogeneous medium with (a) tissue being of Type III and (b) tissue being of Type IV as defined in Table 1.

contrast between the inclusions and tissue, multiple reflections occur between the inclusions. These reflections contaminate the dominant reflection from the inclusion, affecting the image quality. Figure 3(b) shows the MR image when the tissue is of Type IV. In this case, the two inclusions are spatially resolved despite a smaller dielectric contrast between the inclusions and tissue. This is because the increase in the dielectric properties of the tissue effectively increases the electrical size of the inclusions and the image resolution. This example illustrates that the image quality is related to both contrast and resolution. Even though the dielectric contrast is low, good spatial resolution still contributes to the overall quality of an image.

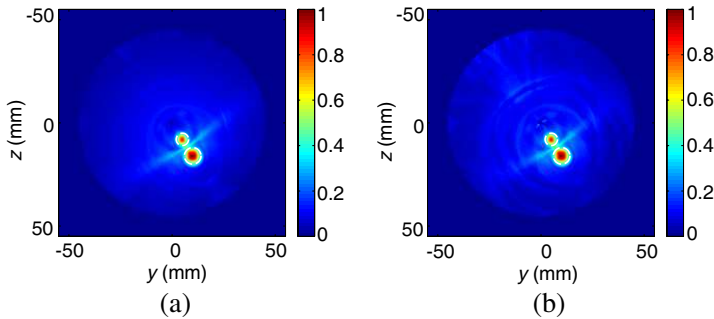


**Figure 4.** MITA images generated with the DAS algorithm attempting to resolve two closely spaced inclusions in a homogeneous medium with (a) tissue being of Type III and (b) tissue being of Type IV as defined in Table 1.

Figure 4 shows the MITA images. As the tissue is almost acoustically homogeneous, variation of the dielectric properties does not affect the acoustic properties. Therefore, the spatial resolution of MITA images is maintained at the level promised by the acoustic wavelength.

### 5.3. A Heterogeneous Breast Model

To compare the imaging capability of the MR and MITA techniques, we test them with a heterogeneous breast model derived from a T1-weighted magnetic resonance image, shown in Figure 5. In the electromagnetic simulation, the pixel intensities are mapped to the Debye parameters by the rule specified in [10]. In the thermoacoustic simulation, the pixel intensities are mapped to the dielectric properties at 550 MHz by the rule specified in [10]. The acoustic heterogeneity is

also modeled by linearly mapping the pixel intensities to the acoustic speed and heat capacity: the largest pixel intensity denoting adipose-dominant tissue is mapped to the smallest acoustic speed and heat capacity.

Figure 6 shows the MITA image generated with the DAS algorithm. The image does not directly resemble the space-dependent parameter shown in Figure 5 due to the introduced acoustic heterogeneity. However, it suggests that the glandular tissue is concentrated to the right half of the model and the several spots correspond to thermoacoustic sources. Figure 7 shows the MR images generated with the DAS algorithm. It is not capable of generating an image that correlates with the tissue properties. The dispersion and heterogeneity of the numerical model pose a challenging task to the MR techniques.

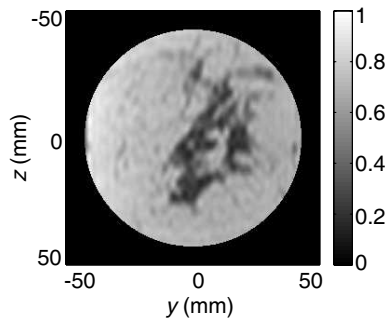


**Figure 5.** A circularly cropped T1-weighted magnetic resonance image.

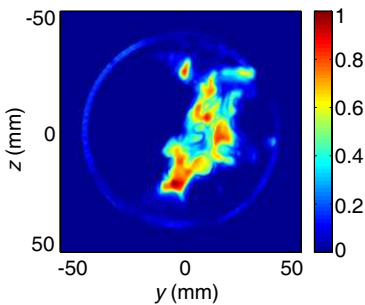


**Figure 6.** MITA image generated with the DAS algorithm.

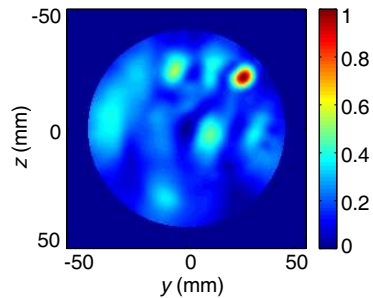


**Figure 7.** MR images generated with the DAS algorithm.

## 6. CONCLUSIONS

We used the DAS algorithm to generate images from the radar and thermoacoustics signals and compared the qualities of the images promised by the MR and MITA techniques. We found that both MR and MITA techniques are capable of imaging dielectric inclusions in a homogeneous medium. Reduced dielectric contrast contributes to the resolution of the images generated by the MR techniques. When applied to a heterogeneous breast model, the MR techniques suffered from the tissue heterogeneity and microwave dispersion. The image from the MITA techniques was able to reveal some spatial detail correlated with the heterogeneity of the tissue.

For future work, we note that the main practical challenge with the MITA technique is to achieve uniform field distribution. This uniformity is desired in order to justify the assumption that the SAR and the conductivity in the tissue are directly correlated as shown in (3). On one hand, the fields in objects with homogeneous structures could be predicted. On the other hand, the heterogeneity of the breast tissue itself and the consequent microwave scattering would challenge the design of the microwave systems to achieve predictable fields.

## REFERENCES

1. Poplack, S. P., K. Paulsen, A. Hartov, P. Meaney, B. Pogue, T. Tosteson, M. Grove, S. Soho, and W. Wells, "Electromagnetic breast imaging: Average tissue property values in women with negative clinical findings," *Radiology*, Vol. 231, 571–580, 2004.
2. Lazebnik, M., L. McCartney, D. Popovic, C. B. Watkins, M. J. Lindstrom, J. Harter, S. Sewall, A. Magliocco, J. H. Booske, M. Okoniewski, and S. C. Hagness, "A large-scale study of the ultrawideband microwave dielectric properties of normal breast tissue obtained from reduction surgeries," *Physics in Medicine and Biology*, Vol. 52, No. 10, 2637–2656, 2007.
3. Lazebnik, M., D. Popovic, L. McCartney, C. B. Watkins, M. J. Lindstrom, J. Harter, S. Sewall, T. Ogilvie, A. Magliocco, T. M. Breslin, W. Temple, D. Mew, J. H. Booske, M. Okoniewski, and S. C. Hagness, "A large-scale study of the ultrawideband microwave dielectric properties of normal, benign and malignant breast tissues obtained from cancer surgeries," *Physics in Medicine and Biology*, Vol. 52, No. 20, 6093–6115, 2007.
4. Halter, R. J., T. Zhou, P. M. Meaney, A. Hartov, R. J. Barth, Jr., K. M. Rosenkranz, W. A. Wells, C. A. Kogel, A. Borsic, E. J. Rizzo, and K. D. Paulsen, "The correlation of in vivo and ex

- vivo tissue dielectric properties to validate electromagnetic breast imaging: Initial clinical experience,” *Physiological Measurement*, Vol. 30, No. 6, S121–S136, Jun. 2009.
5. Li, X., E. J. Bond, B. D. van Veen, and S. Hagness, “An overview of ultra-wideband microwave imaging via space-time beamforming for early-stage breast-cancer detection,” *IEEE Antennas Propag. Mag.*, Vol. 47, No. 1, 19–34, 2005.
  6. Wang, L., “Prospect of photoacoustic tomography,” *Medical Physics*, Vol. 35, 5758–5767, 2008.
  7. Tang, M.-X., D. S. Elson, R. Li, C. Dunsby, and R. J. Eckersley, “Photoacoustics, thermoacoustics, and acousto-optics for biomedical imaging,” *Journal of Engineering in Medicine*, Vol. 224, No. 2, 291–306, 2010.
  8. Diebold, G. J., “Photoacoustic monopole radiation: Waves from objects with symmetry in one, two, and three dimensions,” *Photoacoustic Imaging and Spectroscopy*, No. 1, 3–18, L. V. Wang, Ed., Taylor & Francis Group, Boca Raton, FL, 2009.
  9. Kinsler, L. E., A. R. Frey, A. B. Coppens, and J. V. Sanders, *Fundamentals of Acoustics*, 4th edition, John Wiley & Sons, Inc., New York, NY, 2000.
  10. Zastrow, E., S. K. Davis, M. Lazebnik, F. Kelcz, B. D. van Veen, and S. C. Hagness, “Development of anatomically realistic numerical breast phantoms with accurate dielectric properties for modelling microwave interactions with the human breast,” *IEEE Trans. Biomed. Eng.*, Vol. 55, No. 12, 2792–2800, 2008.
  11. Duck, F. A., *Physical Properties of Tissue: A Comprehensive Reference Book*, Academic Press, San Diego, CA, 1990.
  12. Robinson, M. P., M. J. Richardson, J. L. Green, and A. W. Preece, “New materials for dielectric simulation of tissues,” *Physical and Medical Biology*, Vol. 36, No. 12, 1565–1571, 1991.
  13. Converse, M., E. J. Bond, B. D. van Veen, and S. C. Hagness, “A computational study of ultra-wideband versus narrowband microwave hyperthermia for breast cancer treatment,” *IEEE Trans. Microw. Theory Tech.*, Vol. 54, No. 5, 2169–2180, 2006.
  14. Mast, T. D., “Empirical relationships between acoustic parameters in human soft tissues,” *Acoustics Research Letters Online*, Vol. 37, No. 1, 37–43, 2000.
  15. Prince, J. L. and J. M. Links, *Medical Imaging Signals and Systems*, Prentice Hall, Inc., Upper Saddle River, NJ, 2006.
  16. Werner, J. and M. Buse, “Temperature profiles with respect to inhomogeneity and geometry of the human body,” *Journal of*

- Applied Physiology*, Vol. 63, No. 3, 1110–1118, 1988.
17. Erdmann, B., J. Lang, and M. Seebass, “Optimization of temperature distributions for regional hyperthermia based on a nonlinear heat transfer model,” *Annals of the New York Academy of Sciences*, Vol. 858, 36–46, 1998.
  18. Guo, B., J. Li, H. Zmuda, and M. Sheplak, “Multifrequency microwave induced thermal acoustic imaging for breast cancer detection,” *IEEE Trans. Biomed. Eng.*, Vol. 54, 2000–2010, 2007.
  19. Johnson, D. H. and D. E. Dudgeon, *Array Signal Processing: Concepts and Techniques*, Prentice Hall, Inc., Upper Saddle River, NJ, USA, 1993.
  20. Fear, E. C., X. Li, S. Hagness, and M. A. Stuchly, “Confocal microwave imaging for breast cancer detection: Localization of tumours in three dimensions,” *IEEE Trans. Biomed. Eng.*, Vol. 49, No. 8, 812–822, 2002.
  21. Sacks, Z. S., D. M. Kingsland, R. Lee, and J. F. Lee, “Perfectly matched anisotropic absorber for use as an absorbing boundary condition,” *IEEE Trans. Antennas Propag.*, Vol. 43, 12, 1995.